Electronic Supplementary Information (ESI).

High-performance fuel cell cathodes exclusively containing atomically dispersed iron active sites

Hanguang Zhang,[a] Hoon T. Chung,[b] David A. Cullen,[c] Stephan Wagner,[d] Ulrike I. Kramm,[d] Karren L. More,[e] Piotr Zelenay,[b,*] and Gang Wu[a,*]

[a] Department of Chemical and Biological Engineering, University at Buffalo, The State University of New York, Buffalo, New York 14260, United States

[b] Materials Physics & Applications Division, Los Alamos National Laboratory, Los Alamos, New Mexico 87545, United States

[c] Materials Science and Technology Division, Oak Ridge National Laboratory, Oak Ridge, Tennessee 37831, United States

[d] Technische Universität Darmstadt, Department of Materials- and Earth Sciences and Department of Chemistry, 64287 Darmstadt, Germany

[e] Center for Nanophase Materials Sciences, Oak Ridge National Laboratory, Oak Ridge, Tennessee 37831, United States

Corresponding authors:

E-mail addresses: gangwu@buffalo.edu (G.W.) and zelenay@lanl.gov (P.Z.)

Figures S1 to S15;

Table S1-S4

Experimental details:

Catalyst synthesis

Fe content is given in this work in terms of atomic percent of Fe versus the total metal (Fe+Zn) content in the synthesis of catalyst precursor from 0.05% to 9.0 at.%. The synthesis of 1.5Fe-ZIF catalyst, i.e., the catalyst derived from precursor with 1.5 at.% Fe content, is given here as an example: Zinc nitrate hexahydrate (3.39 g) and iron nitrate nonahydrate (80 mg) were dissolved in 500 mL methanol in a round-bottom flask, followed by addition of 500 mL methanol solution of 2-methylimidazole (3.94 g). The obtained mixture were then kept at 60 °C for 24 h. The resulting suspension was separated by centrifuging at 8700 rpm to collect the precipitants, then washed with ethanol three times. The thus obtained catalyst precursor was dried at 60 °C in a vacuum oven for 8 h, before being heat-treated in a tube furnace at 1100 °C under N_2 for 1 h to obtain final catalyst (1.5Fe-ZIF in this example). The ZIF-8 derived Fe-free catalyst follows the same synthetic procedure above except for the addition of iron nitrate nonahydrate.

Material characterization

Atomic-resolution micrographs were obtained using a Nion UltraSTEM U100 microscope operated at 60 keV and equipped with a Gatan Enfina electron energy loss spectrometer (EELS). Bright field (BF) and high-angle annular dark-field (HAADF) micrographs were recorded in image pairs. EEL spectra to confirm the composition of Fe sites and clusters were obtained after eliminating data noise using the open source Hyperspy python library. Catalyst morphology was also studied using scanning electron microscopy (SEM) on a Hitachi SU 70 microscope operating at 5 kV. The crystal phases in the samples were identified using powder X-ray diffraction (XRD) on a Rigaku Ultima IV diffractometer with Cu K-α X-rays. X-ray photoelectron spectroscopy (XPS) was performed using a Kratos AXIS Ultra DLD XPS system equipped with a hemispherical energy analyzer and a monochromatic Al Kα source. The high-resolution of N1s spectra were fitted with four types of N bonding, including pyridinic N (398.6 eV), pyrrolic N (399.6 eV), graphitic N (401.1 eV) and oxidized N (402.6 eV and 403.8 eV). The elemental Fe content in precursors was determined by inductively coupled plasma (ICP), after complete digestion of precursors in 65% nitric acid. The N_2 isothermal adsorption/desorption was recorded at 77 K using a Micromeritics TriStar II BET instrument. Samples were degassed at 150 °C for 5 h under vacuum prior to nitrogen physisorption measurements. Mößbauer spectroscopy was performed in transmission mode at room temperature using a Co^{57}/Rh source. Data were collected with a scintillation detector and calibration of the velocity axis was made with respect to α–Fe foil. The Raman spectra of catalysts coated on glass slides were recorded with a wavelength of 514 nm laser at ambient condition by the Renishaw Raman system.

Electrochemical measurements

All electrochemical measurements were performed using a CHI Electrochemical Station (Model 760b) in a conventional three-electrode cell at room temperature. A glassy carbon rotating disk electrode (GC-RDE) was used as the working electrode. Each catalyst was mixed with isopropanol and 5 wt% suspension of Nafion® in alcohols to produce catalyst ink that was drop-cast onto the GC-RDE and air-dried at 60 °C. Cyclic voltammetry (CV) was then recorded in N_2-saturated 0.5 M H_2SO_4 electrolyte at a scan rate of 20 mV/s to

estimate the electrochemically accessible surface area from the double layer capacitance, assuming a capacitance 30 μF per cm^2 of the catalyst surface (These M-N-C catalysts contain almost 95% of carbon.), following the approach in our previous work[52]. The ORR activity and four-electron selectivity were determined from rotating ring disc electrode (RRDE) measurements, performed in O_2-saturated 0.5 M H_2SO_4 at room temperature and rotation rate of 900 rpm. A graphite rod was used as the counter electrode. $Hg/HgSO_4$ in saturated K_2SO_4, was the reference electrode. The catalyst loading RDE/RRDE testing was 0.8 mg/cm^2, except in the loading dependence studies. ORR steady-state polarization plots were recorded using potential steps of 0.05 V at time intervals of 30 s in the potential range from 1.0 to 0 V *vs*. RHE. The potential of platinum ring on RRDE was kept at 1.2 V *vs*. RHE during recording ORR polarization curves. The hydrogen peroxide yield was calculated from the recorded ring (I_r) and disk current (I_d) using the following equation where N=0.36 is collection efficiency:

$$H_2O_2 \text{ yield } (\%) = 200I_r/(I_r+NI_d)$$

Two accelerated stress testing approaches (potential cycling and constant potential holding) are both employed to evaluate the stability of catalysts in RRDE. The potential cycling was carried out from 0.6 to 1.0 V *vs*. RHE for 40,000 cycles in an oxygen saturated 0.5 M H_2SO_4. The polarization curves were recorded every 10,000 cycles. Chronoamperometry was used to conduct constant potential holding at 0.85 V *vs*. RHE for 100 h in an oxygen saturated 0.5 M H_2SO_4. The corresponding polarization curves were taken every 10 h.

Fuel cell testing

Catalyst ink containing 35 wt% of Nafion® was made by ultrasonically mixing the catalyst, isopropanol, de-ionized water, and 5% Nafion® suspension in alcohols at a 1:12:12:11 weight ratio for three hours. The inks were applied to the membrane by brushing until the cathode catalyst loading of ~4.0 mg cm^{-2} was reached. A commercial Pt-catalyzed gas diffusion electrode (GDE, 0.2 mg_{Pt}/cm^2, IRD Fuel Cells) was used at the anode. The cathode gas diffusion layer and the anode GDE were hot-pressed onto a Nafion® 212/211 membrane at 125°C for 5 minutes. The geometric surface area of the membrane electrode assembly (MEA) was 5.0 cm^2. Fuel cell testing was carried out in a single-cell fuel cell with a single-serpentine flow channels. Pure hydrogen and air/oxygen humidified at 80 °C were supplied to the anode and cathode, respectively, at a flow rate of 200 mL/min. The total partial pressure of gases at both electrodes was 1.0 bar. Fuel cell polarization plots were recorded using standard fuel cell test stations (Fuel Cell Technologies Inc.) in a voltage control mode. Chronoamperometry was employed to record the current change during the constant potential holding at 0.7 V or 0.55 V for 118 h and 95 h in the H_2-air cell with the same condition used for testing polarization curves.

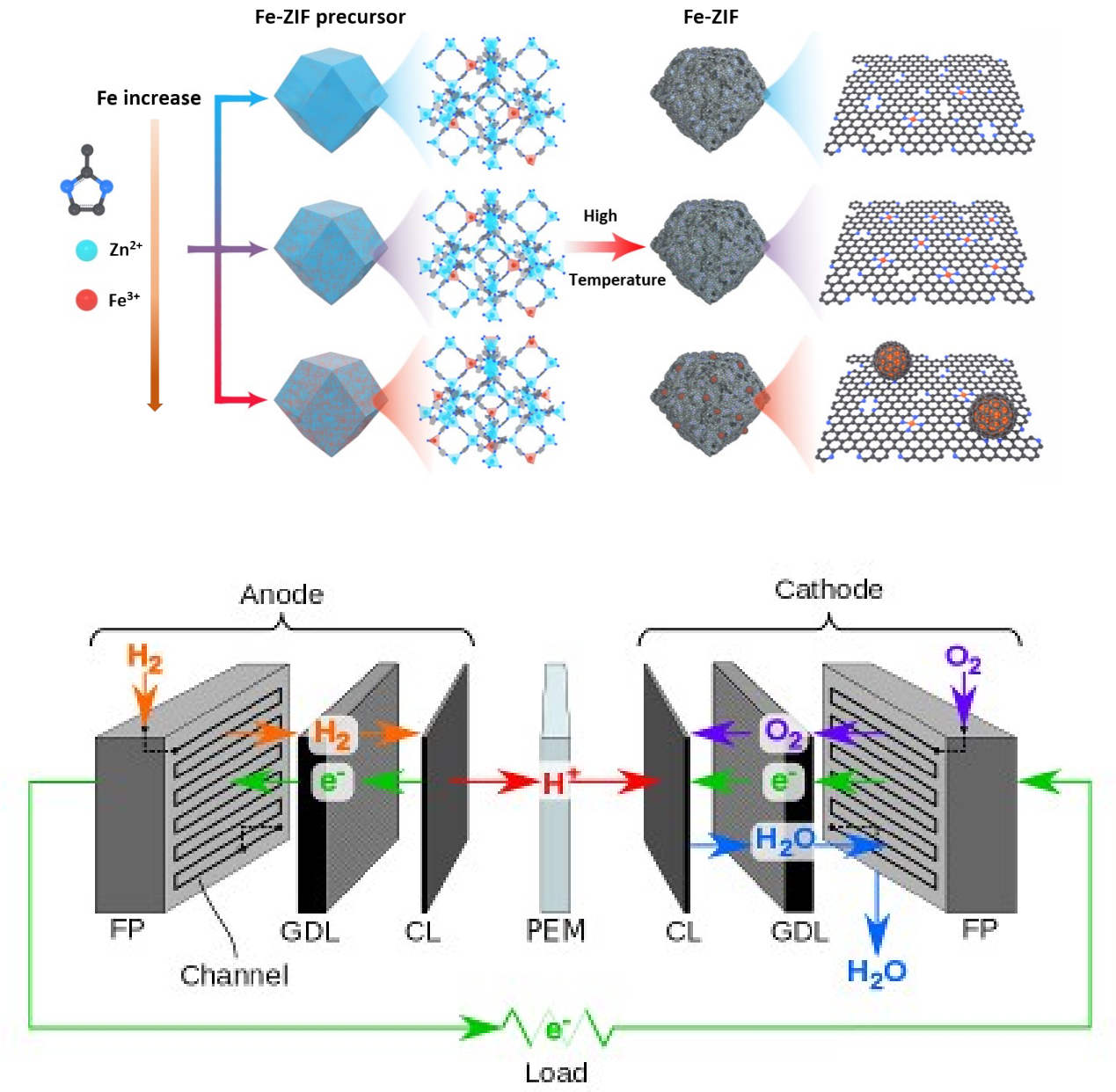

Figure S1. (*Top*) Schematic illustration of synthesis of precursor Fe-ZIF and their derived catalysts Fe-ZIF with various doped Fe content in ZIF-8 precursors. (*Bottom*) Basic An assembled fuel cell hardware used for PEFC tests (*Reproduced from fuel cell training materials of Los Alamos National Laboratory*)

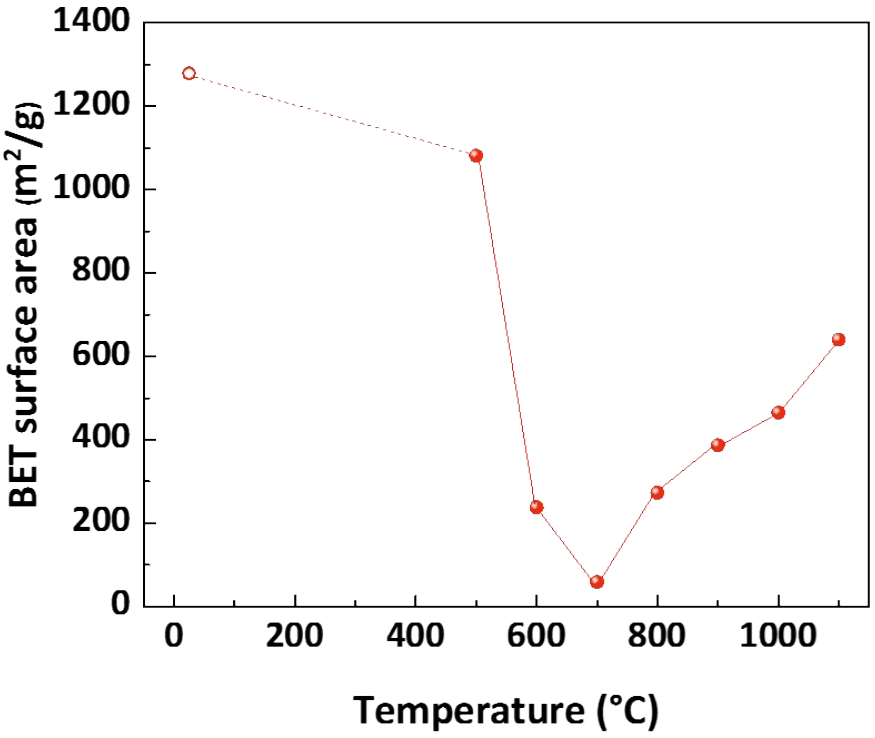

Figure S2. The BET surface area of 1.5Fe-ZIF as a function of the heat-treatment temperature in the range from 500 °C to 1100 °C. The BET surface area of the precursor is shown with an open circle.

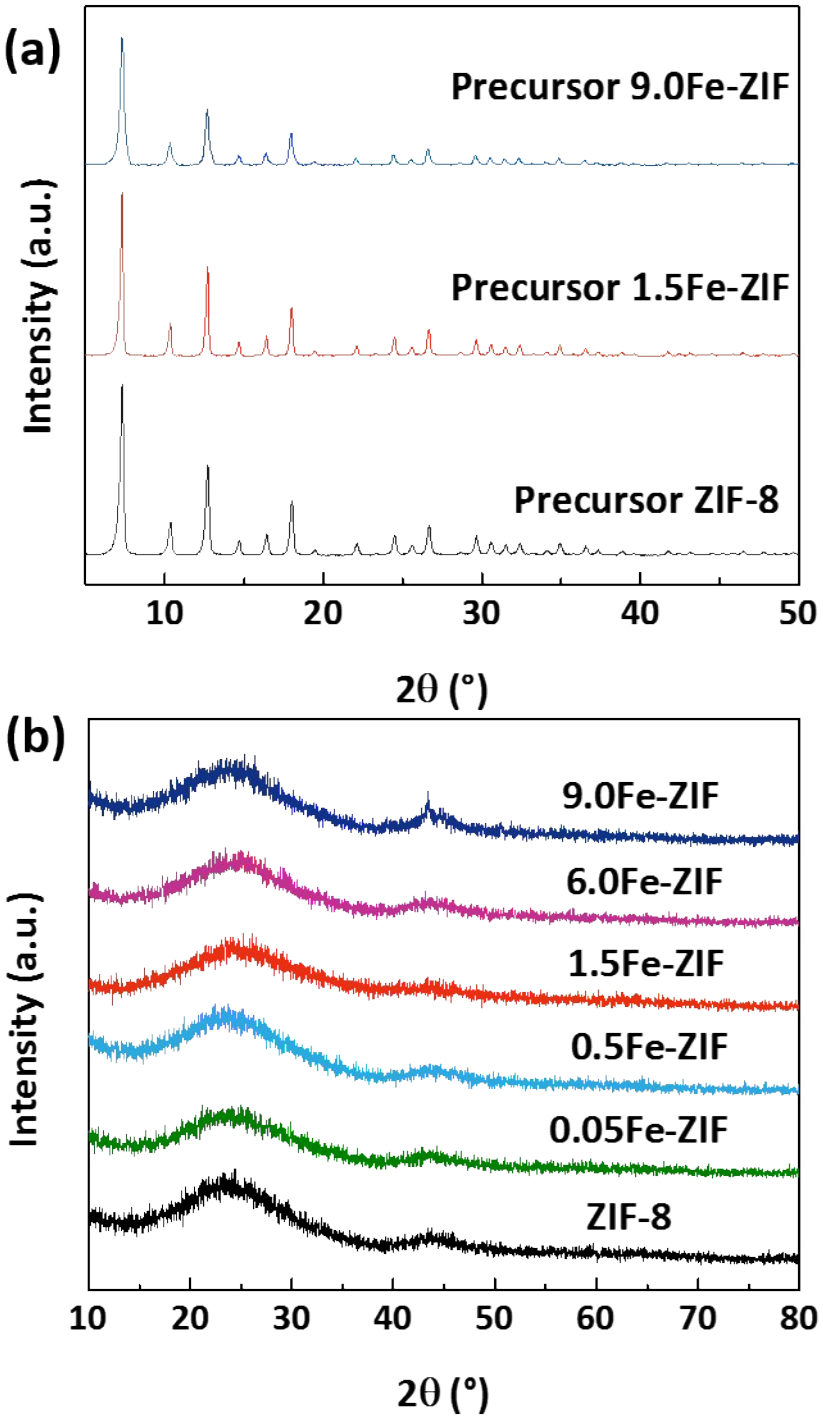

Figure S3. XRD patterns for **(a)** Fe-free and Fe-doped ZIF precursors and **(b)** ORR catalysts obtained after single heat-treatment at 1100 °C as a function of the doped Fe content.

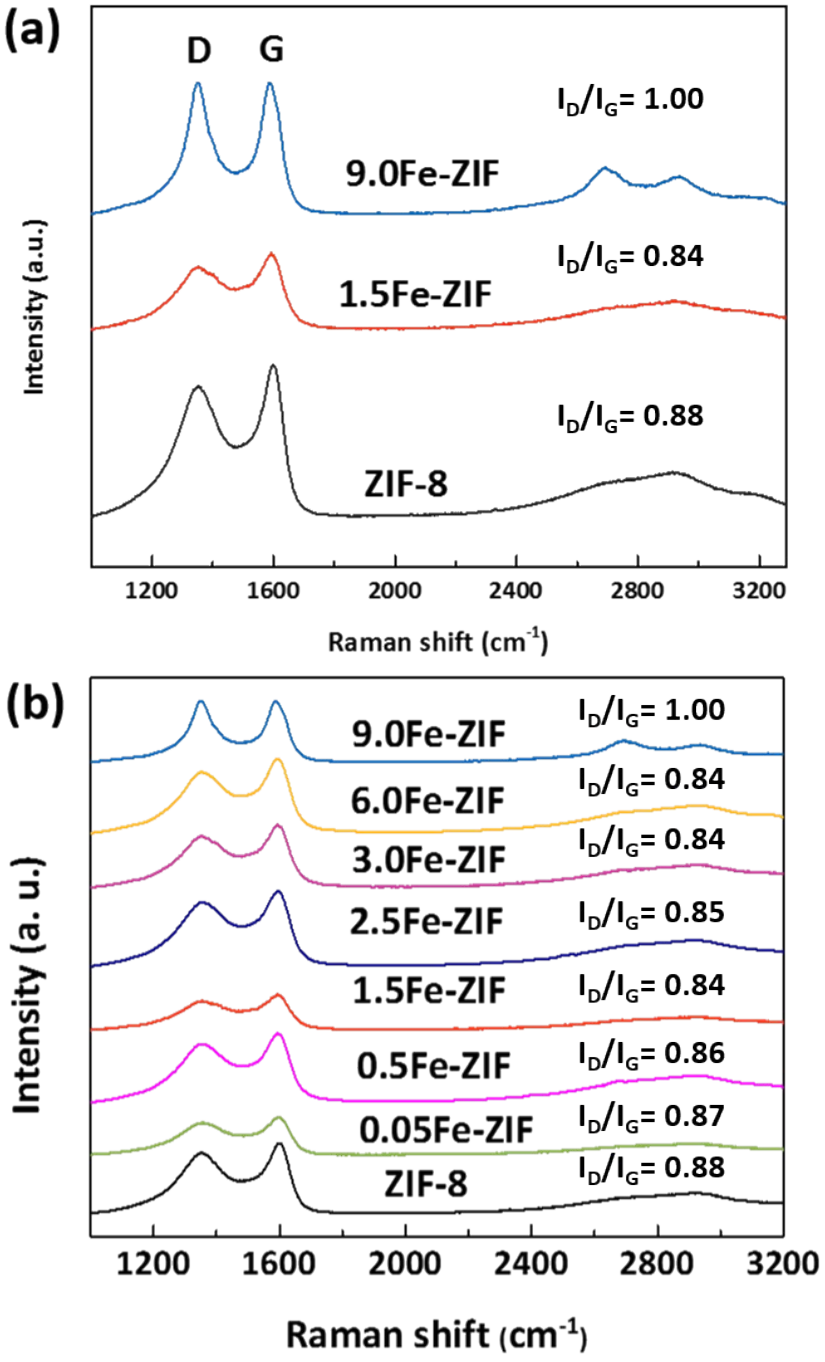

Figure S4. Raman spectroscopy of the Fe-ZIF catalysts (pyrolyzed at 1100 °C) with different Fe content in the precursor. **(a)** Raman spectra for three selected catalysts (Fe-free and two Fe-containing ones); **(b)** Raman spectra for all studied catalysts.

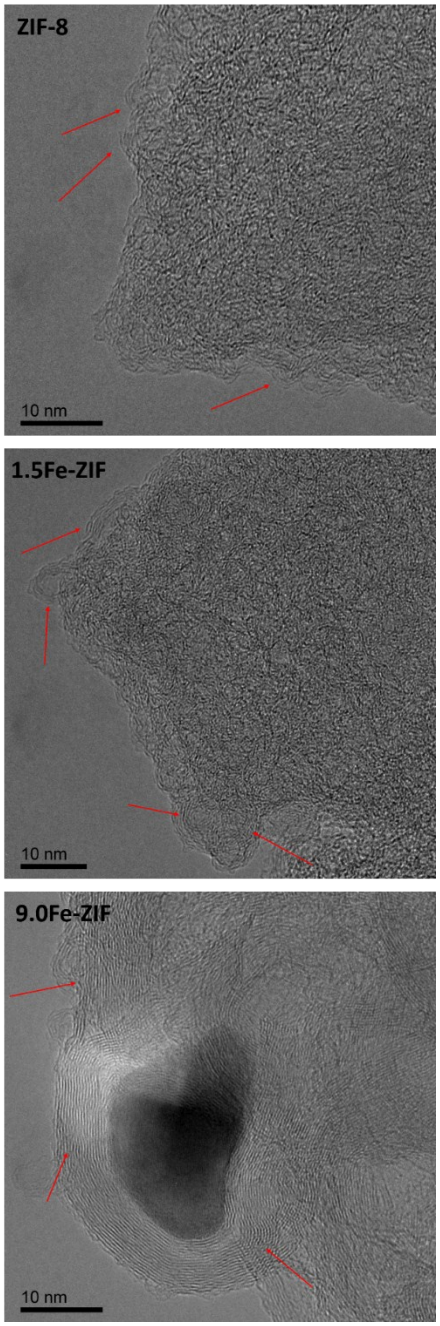

Figure S5. The HR-TEM images of the carbon structure of catalysts derived from ZIF-8; 1.5Fe-ZIF, and 9.0Fe-ZIF. Red arrows pointing to different carbon structures present.

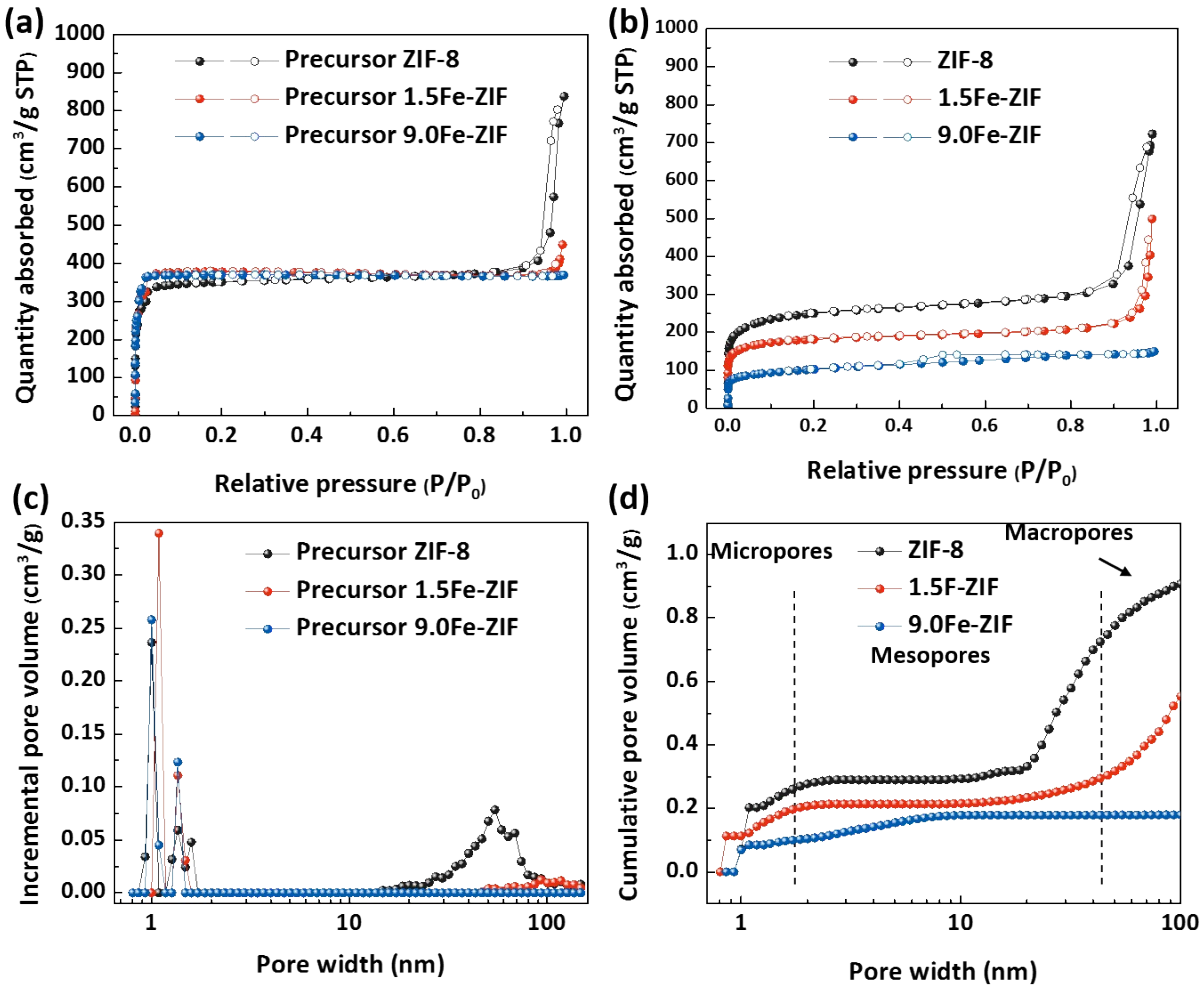

Figure S6. Isothermal N_2 sorption curves for **(a)** ZIF-8, 1.5Fe-ZIF and 9.0Fe-ZIF precursors and **(b)** catalysts derived from these precursors. **(c)** Pore-size distribution plots for ZIF-8, 1.5Fe-ZIF and 9.0Fe-ZIF precursors; **(d)** cumulative pore volume in ZIF-8, 1.5Fe-ZIF and 9.0Fe-ZIF catalysts as a function of the pore width.

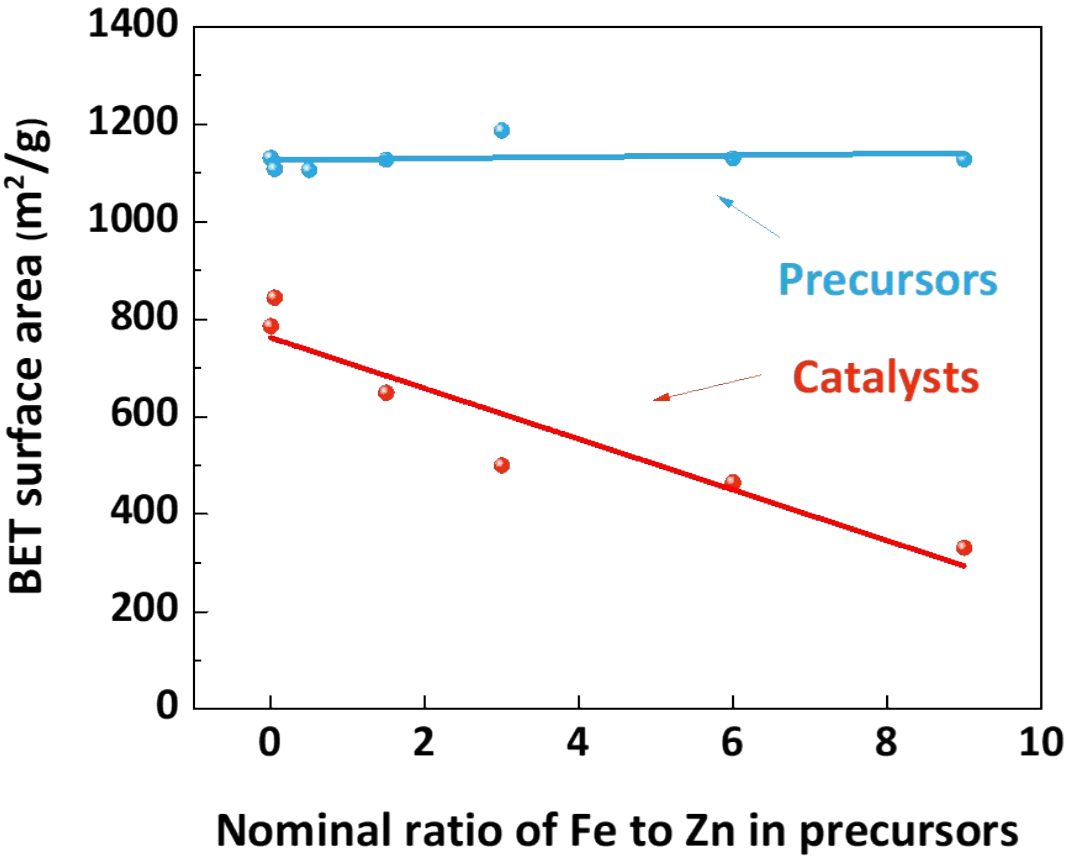

Figure S7. BET surface area of the Fe-doped ZIF precursors and catalysts derived from these precursors as a function of the doped Fe content.

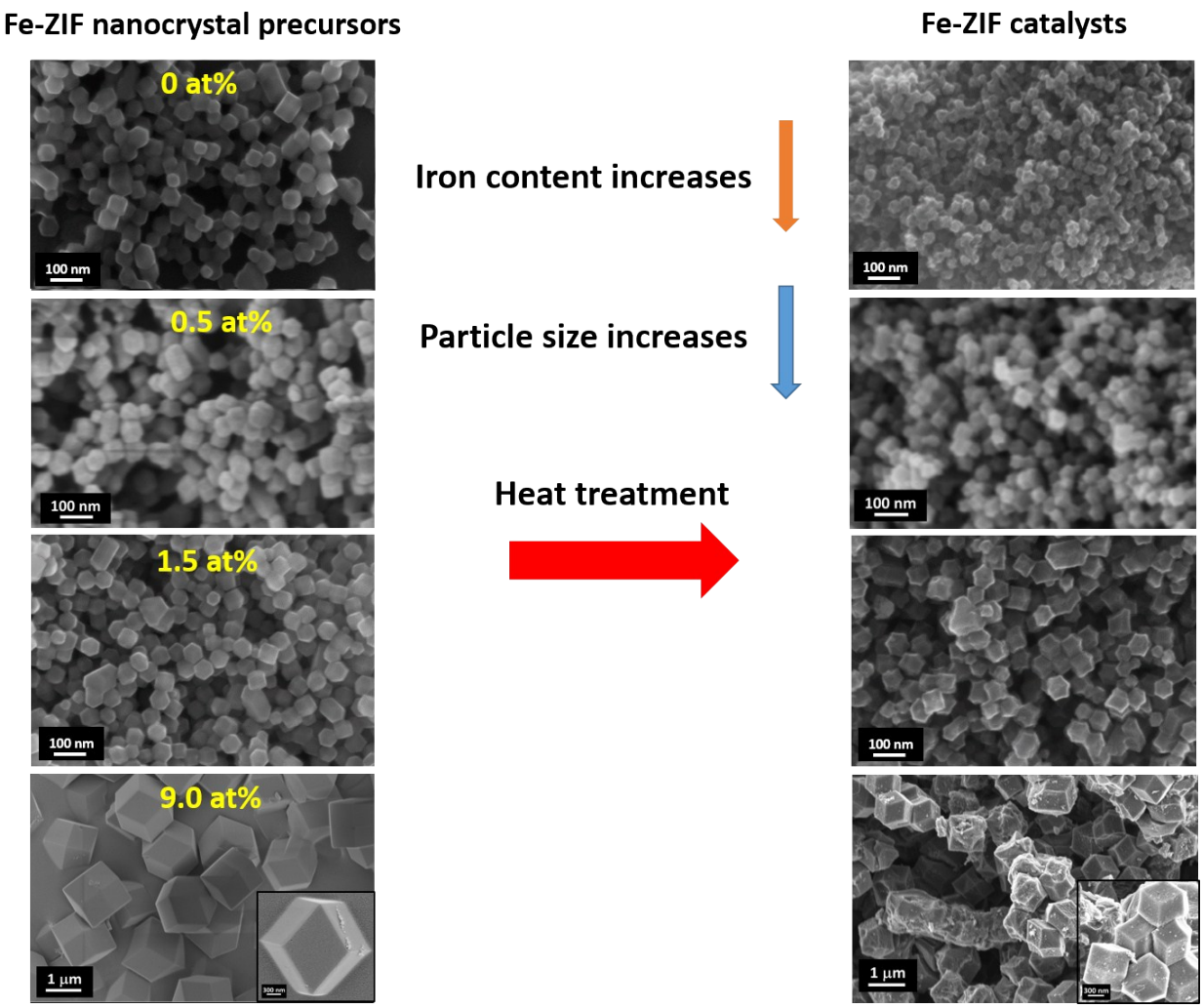

Figure S8. Scanning electron microscopy images of Fe-doped ZIF precursors with various Fe content (left) and of the corresponding catalysts after the heat treatment at 1100 °C (right).

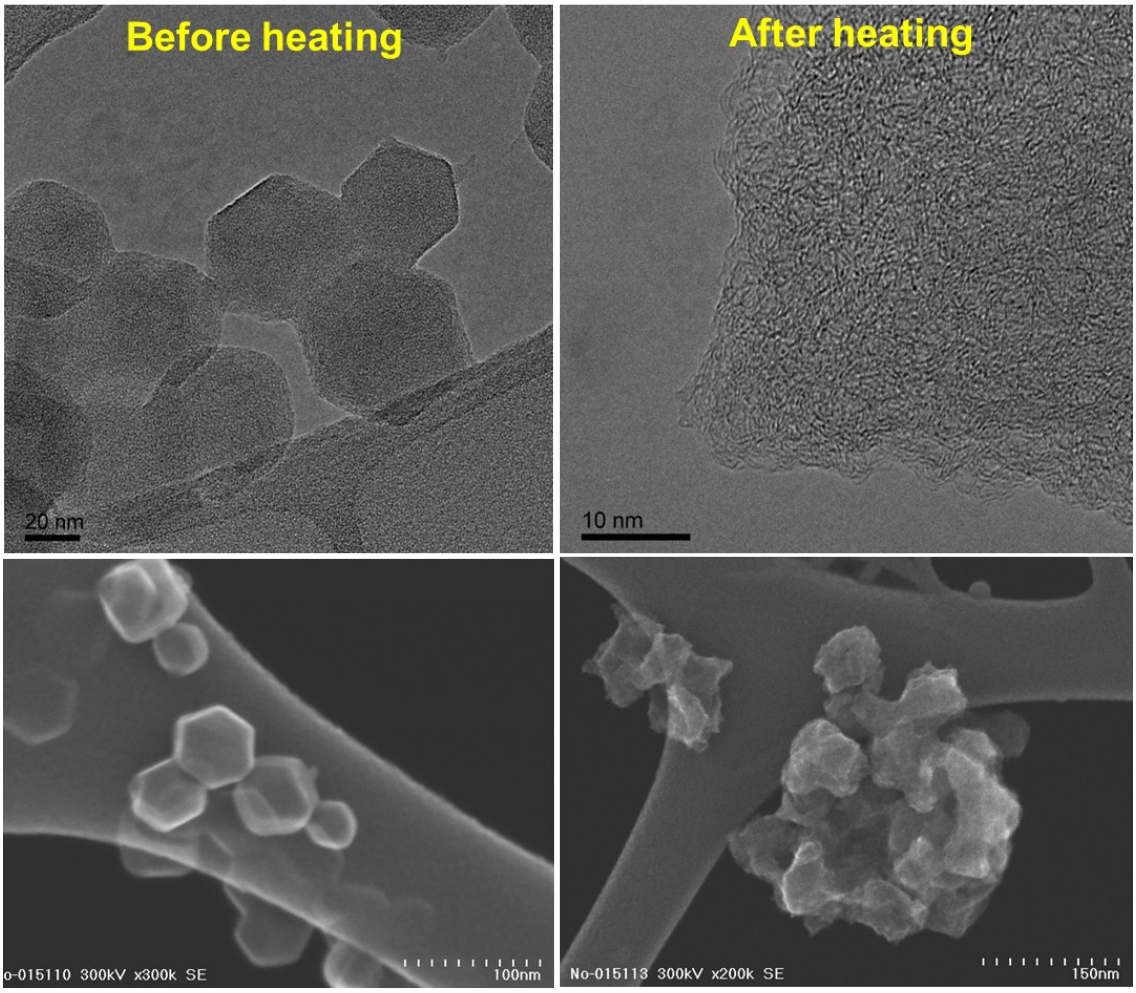

Figure S9. Morphology of the "Fe-free" ZIF-8 precursor and catalyst before and after the heat treatment at 1100 °C.

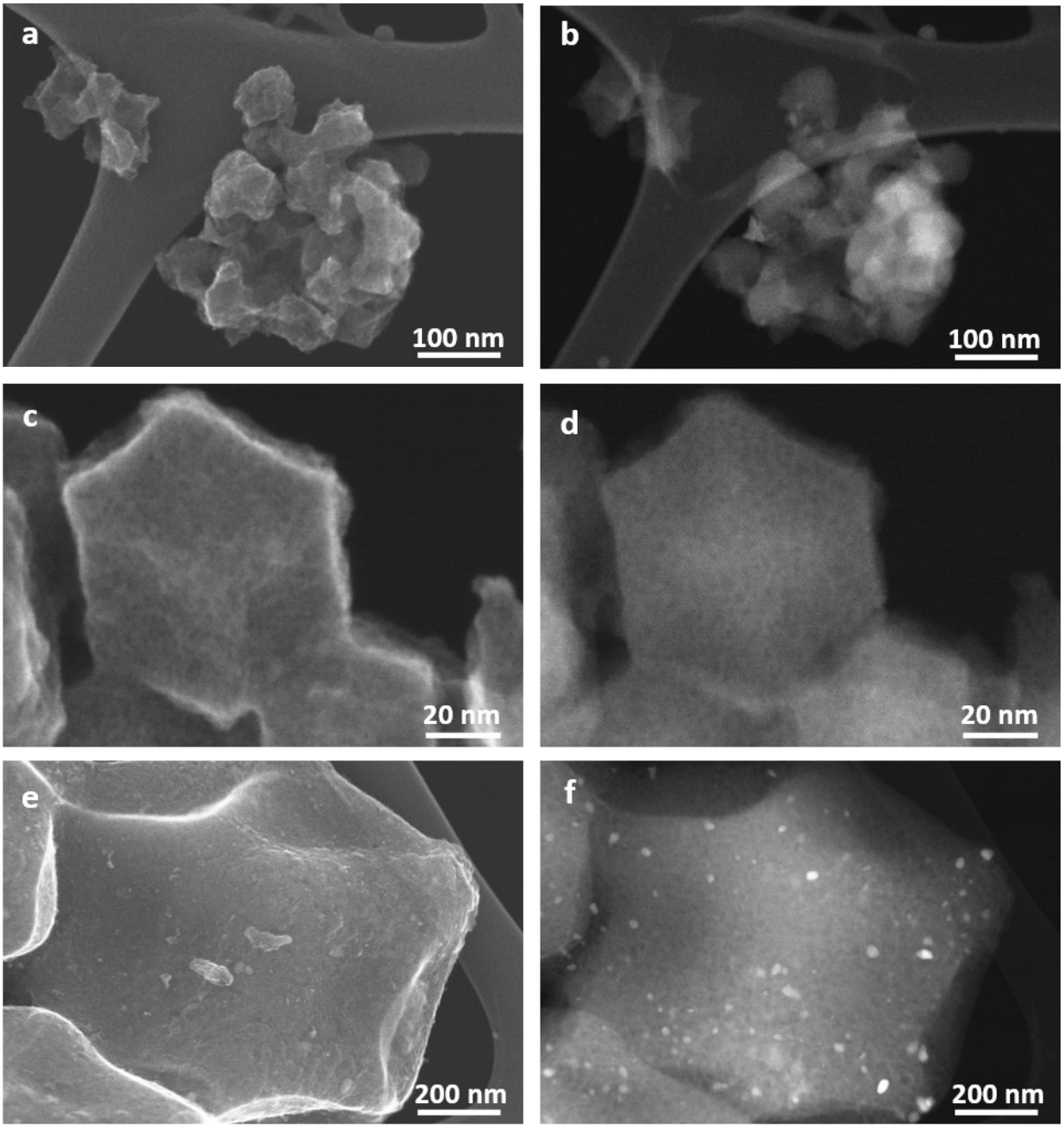

Figure S10. TEM images in bright field mode and in HAADF mode for catalysts derived from **(a, b)** ZIF-8, **(c, d)** 1.5Fe-ZIF, and **(e, f)** 9.0Fe-ZIF.

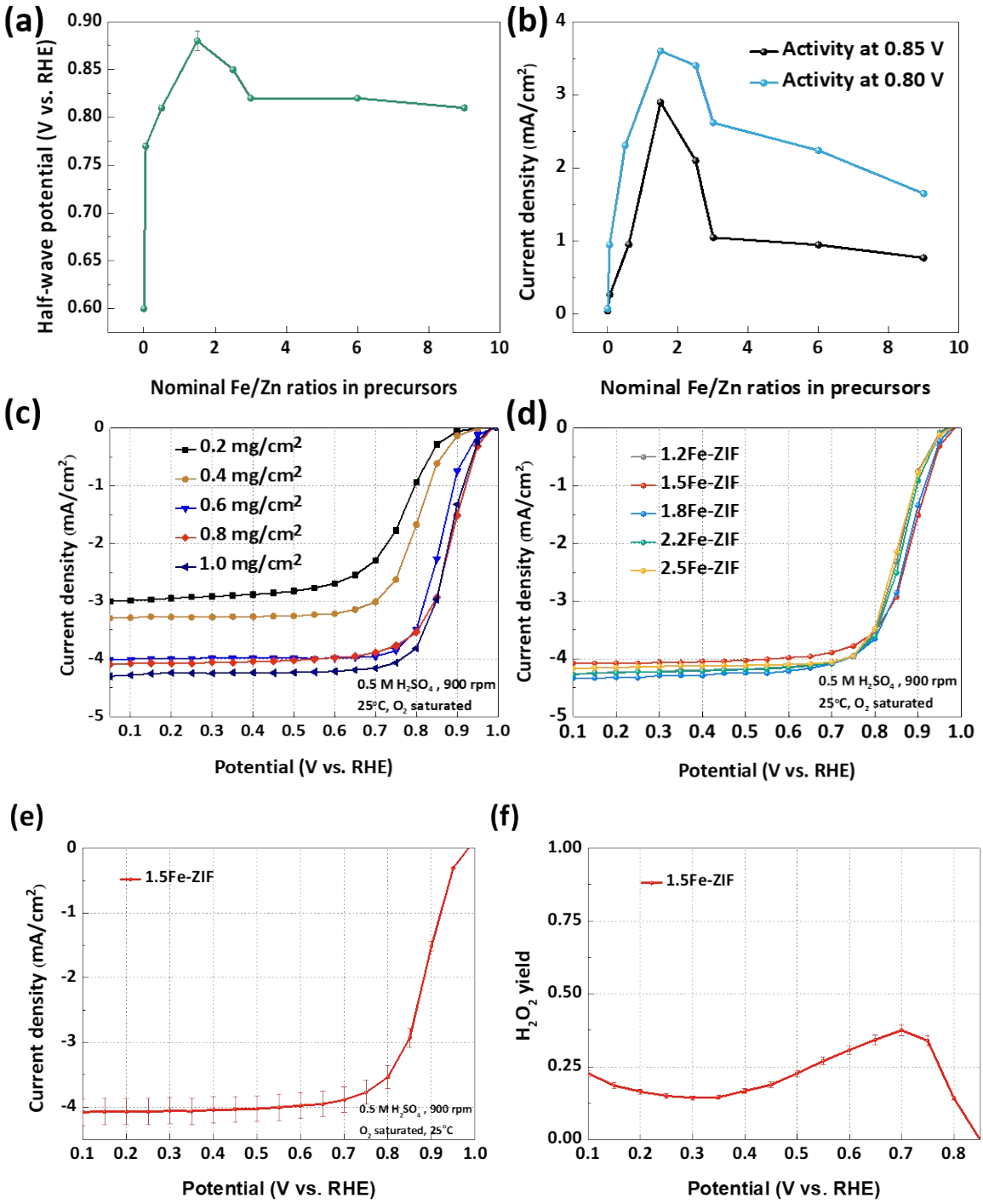

Figure S11. ORR activity of Fe-ZIF catalysts as a function of the doped-Fe content using **(a)** ORR half-wave potential determined in RDE testing at a rotation speed of 900 rpm and **(b)** current density at high potentials of 0.85 V and 0.80 V; catalyst loading of 0.8 mg/cm^2. **(c)** ORR RDE plots for the best performing 1.5Fe-ZIF catalyst at different loadings at the disk. **(d)** ORR RDE plots for Fe-ZIF catalysts with Fe content from 1.2 to 2.5 at%. ORR activity (**e**) and selectivity **(f)** for the best performing Fe-N-C catalysts with error bars.

Table S1. Summary of RDE performance in acidic electrolytes of the most active 1.5Fe-ZIF catalyst in this work and several Fe-N-C catalysts reported in literature.

Catalyst	Electrolyte and disk rotation rate/rpm	Onset potential/V (*vs.* RHE)	Half-wave potential /V (*vs.* RHE)	Current density at 0.9 V (*vs.* RHE) /mA cm^{-2}	Ref.
1.5Fe-ZIF	0.5 M H_2SO_4, 900	0.98	0.88	1.5	This work
$Fe_{0.5}$-900	0.1 M H_2SO_4, 1600	0.99	0.88	1.5	1
$Zn(eIm)_2TPIP$	0.1 M $HClO_4$, 1600	0.91	0.78	0.1	2
Fe/N/C/NF	0.5 M H_2SO_4, 900	0.93	0.80	0.2	3
Fe SAs/N-C	0.1 M $HClO_4$, 1600	0.95	0.75	0.4	4
PAN-Fe-C	0.5 M H_2SO_4, 900	0.93	0.80	0.2	5
(CM+PANI) Fe-C	0.5 M H_2SO_4, 900	0.95	0.80	0.2	6
Fe-N-C	0.1 M $HClO_4$, 1600	0.94	0.84	0.8	7
Fe-PAN-EN-hydrogel	0.5 M H_2SO_4, 900	0.95	0.83	0.8	8
(DFTPP)Fe-Im-CNTS	0.1 M $HClO_4$, 1600	1.05	0.88	2.5	9
pCNT@Fe1.5%@GL-NH_3	0.1 M $HClO_4$, 1600	0.98	0.88	2.0	10

Table S2. Summary of calculation for the maximum mass-based site density, mass-based kinetic current and turnover frequency

Catalysts	Fe /wt%	Fe (D1) /wt%	MSD_{max} /site g_{cat}^{-1}	I_{kin} (0.8 V) /A g_{cat}^{-1}	TOF (0.8 V) /e $s^{-1}site^{-1}$	Ref
1.5Fe-ZIF	2.14[a]	1.24	1.34×10^{20}	45.0	2.14	This work
FePhenMOF-$ArNH_3$	0.5[b]	0.2	2.16×10^{19}	7.78	2.40	12
Fe-N-C-3HT-2AL	6.0[b]	1.33	1.43×10^{20}	21.0	0.92	7

a determined by XPS
b determined by ICP

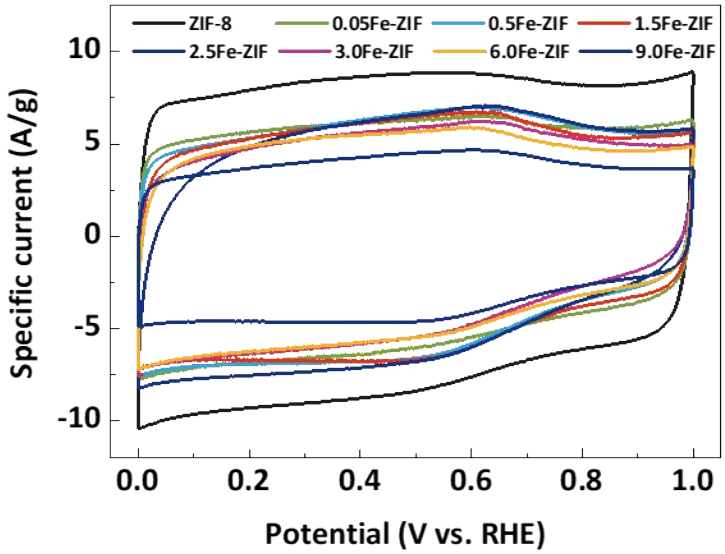

Figure S12. Cyclic voltammetry of Fe-free and Fe-ZIF catalysts in N_2 saturated 0.5 M H_2SO_4

Table S3. Electrochemically accessible surface area of Fe-free and Fe-ZIF-derived catalysts.

Catalysts	Electrochemically accessible surface area (m^2/g)
ZIF-8	795
0.05Fe-ZIF	570
0.5Fe-ZIF	566
1.5Fe-ZIF	556
2.5Fe-ZIF	554
3.0Fe-ZIF	495
6.0Fe-ZIF	488
9.0Fe-ZIF	388

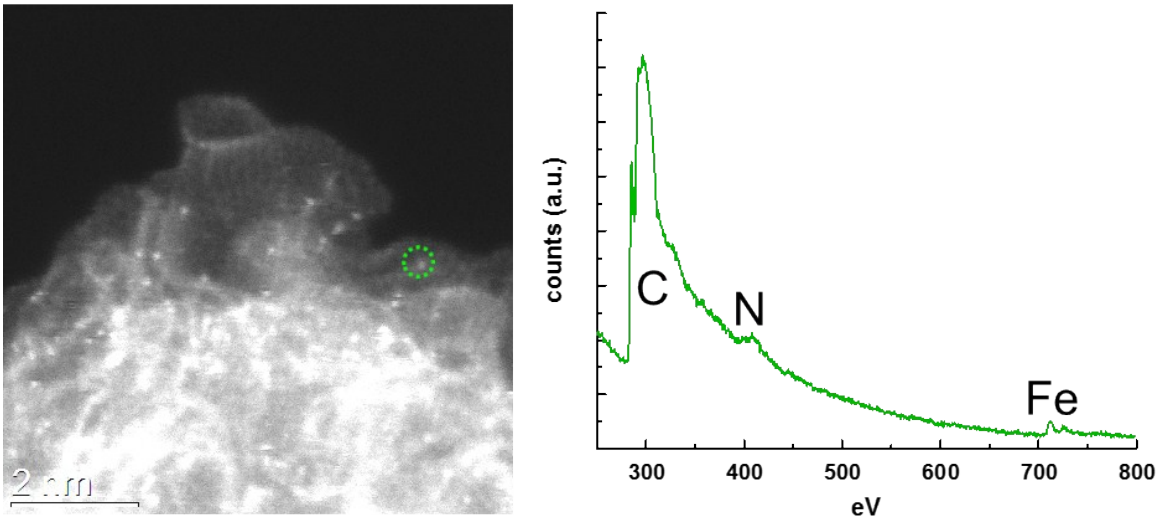

Figure S13. The HAADF-STEM image of the 1.5Fe-ZIF catalyst after the cycling stability test and the electron energy loss (EEL) spectra from the specified point cycled in green.

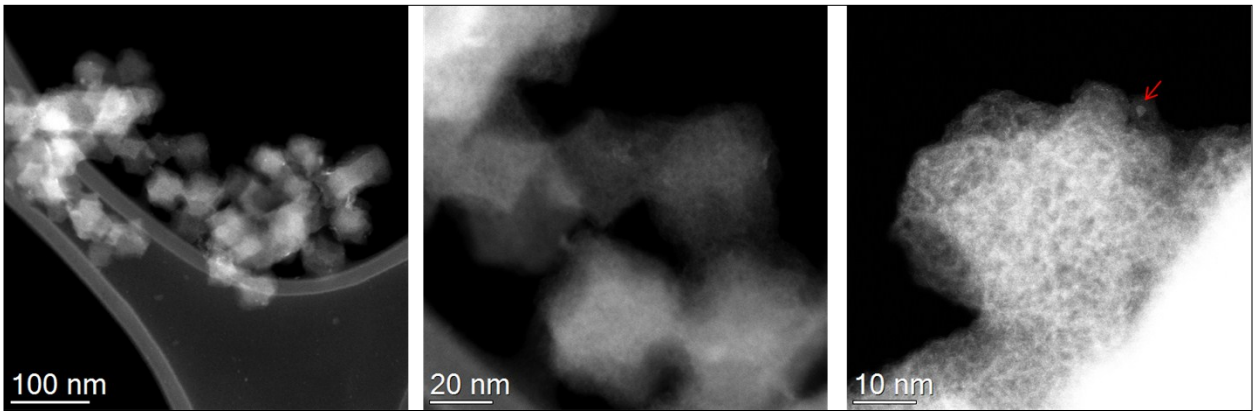

Figure S14. Carbon particle morphology in 1.5Fe-ZIF catalysts after potential cycling from 0.6 to 1.0 V in O_2-saturated 0.5 M H_2SO_4 solution for 30,000 cycles.

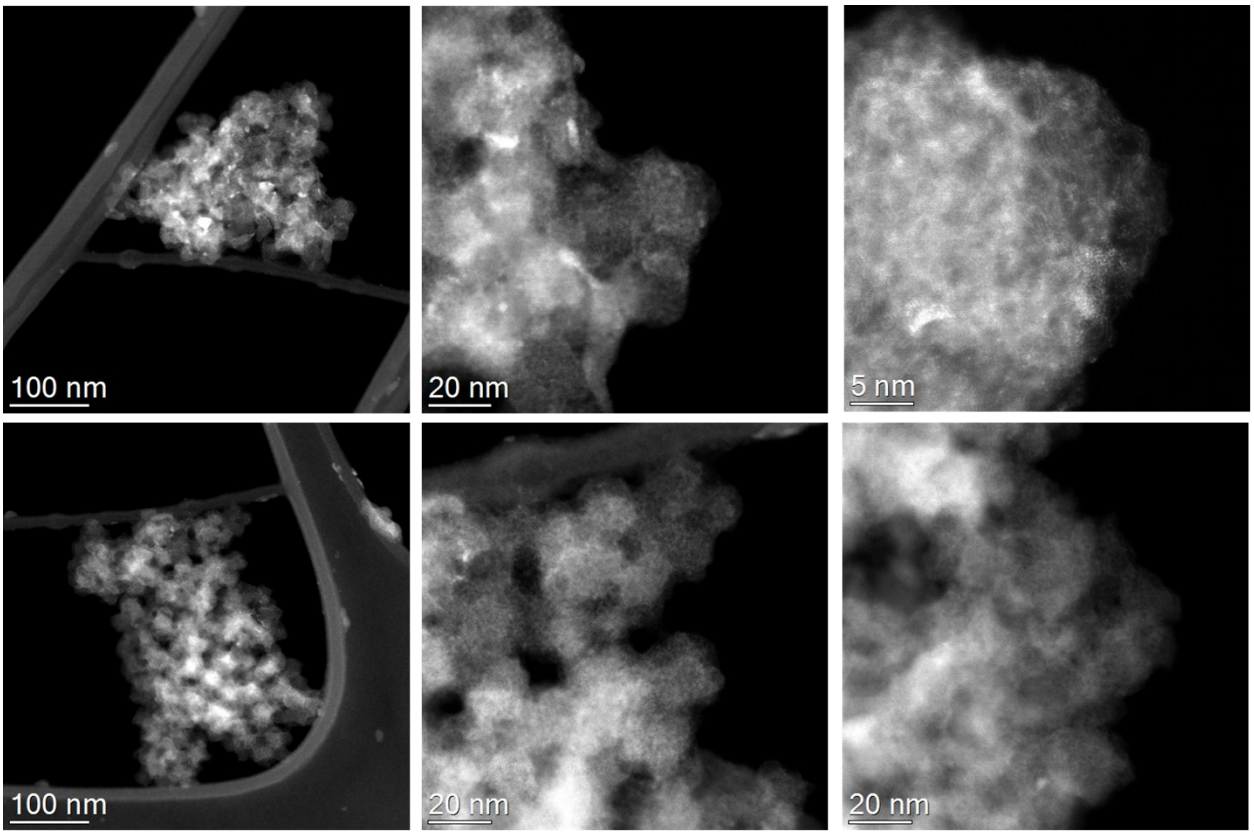

Figure S15. Carbon particle morphology of the 1.5Fe-ZIF catalyst after the durability test at a constant potential of 0.85 V for 100 hours. Micrographs highlight the appearance of Fe clusters and rounding of the carbon particles that implies carbon corrosion.

Table S4. Summary of activity and durability for PGM-free catalysts at RDE and fuel cells

Catalysts	Times of heat treatment	Acid-leaching	RDE tests in acid electrolyte		MEA tests				Ref.
			Activity	Stability	Activity		Durability		
			$E_{1/2}$ /V vs. RHE	Loss in $E_{1/2}$ /V vs. RHE (cycle numbers from 0.6-1.0 V vs. RHE)	Current density @0.8 V /mA and ($P_{oxidant}$)	Peak power density /W	Current retention /%, testing voltage /V, and duration /h	Power density[d] /W, (testing voltage /V, and duration/h)	
1.5Fe-ZIF	1	No	0.88	20 mV (10,000 cycles) 30 mV (40,000 cycles)	75[b] (1 bar); 120[c] (1 bar)	0.36[b] 0.67[c]	48[b] (0.7 V, 118 h) 51[b] (0.55 V, 95 h)	0.15[b] (0.55 V, 95 h)	This work
$Fe_{0.5}$-950	2	No	0.88	-	150[c] (1.5bar)	-	46[c] (0.5 V, 50 h)	0.25[c] (0.5 V 50 h)	1
1/20/80-Z8-1050°C-15	2	No	-	-	400[c] (1.5 bar)	0.91[c]	43[b] (0.5 V, 100h) 22[c] (0.5 V 100h)	0.13[b] (0.5 V 100 h) 0.11[c] (0.5 V 20 h)	11
Fe/N/CF	3	Yes	0.80	8 mV (35,000 cycles)[a]	250[c] (2 bar)	0.90[c]	28[c] (0.5 V,100h)	0.14[c] (0.5 V, 100h)	3
FePhen MOF–$ArNH_3$	2	Yes	0.78	-	50[b] (2.5 bar)	0.40[b]	-	-	12
SA-Fe/NG	1	Yes	0.80	8m V (5,000 cycles)	100[c] (2.5 bar)	0.82[c]	23[c] (0.5 V, 20 h)	0.13[c] (0.5 V, 20h)	13
pCNT@Fe1.5%@GL-NH_3	3	No	0.88	80 mV (10,000 cycles)	-	-	-	-	10

a Stability test in N_2 saturated acids. Other catalysts were tested in O_2 saturated acids.

b H_2-air cell

c H_2-O_2 cell

d Calculated power density at the voltage for durability test

References

1 A. Zitolo, V. Goellner, V. Armel, M.-T. Sougrati, T. Mineva, L. Stievano, E. Fonda and F. Jaouen, Nature Materials, 14, 937.

2. D. Zhao, J.-L. Shui, L. R. Grabstanowicz, C. Chen, S. M. Commet, T. Xu, J. Lu and D.-J. Liu, Advanced Materials, 2014, 26, 1093-1097.

3. J. Shui, C. Chen, L. Grabstanowicz, D. Zhao and D. J. Liu, Proceedings of the National Academy of Sciences of the United States of America, 2015, 112, 10629-10634.

4. J. Wang, Z. Huang, W. Liu, C. Chang, H. Tang, Z. Li, W. Chen, C. Jia, T. Yao, S. Wei, Y. Wu and Y. Li, Journal of the American Chemical Society, 2017, DOI: 10.1021/jacs.7b10385.

5. G. Wu, K. L. More, C. M. Johnston and P. Zelenay, Science, 2011, 332, 443-447.

6. H. T. Chung, D. A. Cullen, D. Higgins, B. T. Sneed, E. F. Holby, K. L. More and P. Zelenay, Science, 2017, 357, 479-484.

7. N. R. Sahraie, U. I. Kramm, J. Steinberg, Y. Zhang, A. Thomas, T. Reier, J.-P. Paraknowitsch and P. Strasser, Nature Communications, 2015, 6.

8. Z. Qiao, H. Zhang, S. Karakalos, S. Hwang, J. Xue, M. Chen, D. Su and G. Wu, Applied Catalysis B: Environmental, 2017, 219, 629-639.

9. W. Ping-Jie, Y. Guo-Qiang, N. Yoshinori and L. Jin-Gang, Angewandte Chemie International Edition, 2014, 53, 6659-6663.

10. S. H. Ahn, X. Yu and A. Manthiram, Advanced Materials, 2017, 29, 1606534.

11. Proietti, E.; Jaouen, F.; Lefèvre, M.; Larouche, N.; Tian, J.; Herranz, J.; Dodelet, J.-P. Nat Commun 2011, 2, 416.

12. Li, J.; Ghoshal, S.; Liang, W.; Sougrati, M.-T.; Jaouen, F.; Halevi, B.; McKinney, S.; McCool, G.; Ma, C.; Yuan, X.; Ma, Z.-F.; Mukerjee, S.; Jia, Q. *Energ. Envi. Sci.* 2016, *9*, 2418.

13. Yang, L.; Cheng, D.; Xu, H.; Zeng, X.; Wan, X.; Shui, J.; Xiang, Z.; Cao, D. Proceedings of the National Academy of Sciences 2018, 115, 6626.